ASME Journal of Manufacturing Science and Engineering
Online journal at:
https://asmedigitalcollection.asme.org/manufacturingscience

**Yangyuan Li**
Department of Mechanical Engineering,
Texas A&M University,
College Station, TX 77840
e-mail: liyangyuan@tamu.edu

**Cong-Yue Wu**
Department of Mechanical Engineering,
National Chung Hsing University,
Taichung 402, Taiwan
e-mail: da853127@gmail.com

**Ming-Chyuan Lu**
Department of Mechanical Engineering,
National Chung Hsing University,
Taichung 402, Taiwan
e-mail: mclu@dragon.nchu.edu.tw

**Jyhwen Wang**
Department of Engineering Technology
and Industrial Distribution,
Texas A&M University,
College Station, TX 77840
e-mail: jwang@tamu.edu

**Dan Feng**[1]
Department of Mechanical Engineering,
Howard University,
Washington, DC 20059
e-mail: Dan.Feng@howard.edu

# In-Line Monitoring of Balling Phenomenon in Directed Energy Deposition Processes

*We develop two in-line monitoring methods—the contact angle (CA) method and the weighted mask (WM) method—to efficiently detect balling phenomenon in directed energy deposition (DED) processes. These methods are designed to support process developers in controlling the process and minimizing instability. The CA method monitors the melt pool's CA as a direct and explicit indicator for detecting balling, while the WM method generates an evaluation number that reflects the likelihood of balling occurrence in an implicit but faster manner. Experimental validation compares the WM method and an existing acoustic-based audible sound method against the CA method using the same dataset of high-speed videos. Using eight threads of an AMD Ryzen™ 9 7940HS CPU, the CA and WM methods achieved processing speeds of 665 fps and 903 fps, respectively. These results demonstrate that both methods are well-suited for real-time, in-line feedback control in DED additive manufacturing, enabling improved defect detection, adaptive process control, and optimization of DED parameters.* [DOI: 10.1115/1.4070451]

*Keywords: directed energy deposition (DED), additive manufacturing, balling phenomenon, image processing, in-line monitoring, laser processes, metrology, sensing, monitoring, and diagnostics*

## 1 Introduction

Directed energy deposition (DED), a metal additive manufacturing technique, holds significant application potential in the fields of aerospace [1–3], transportation [4–6], biomedical implants [7–9], and remanufacturing [10–12]. Its primary advantage lies in the ability to produce high-performance and large-scale components and the compatibility to fabricate composite structures [13–17]. The rapid heating and cooling rates inherent to the DED process also contribute to the high strength of the manufactured components [18]. Furthermore, compared to traditional subtractive manufacturing methods, DED provides higher material efficiency and design flexibility, enabling the production of geometrically complex structures [13–16]. Nevertheless, the DED manufacturing process still faces significant challenges, particularly in optimizing process parameters and controlling defects [13–16,19,20]. The use of high-energy heat sources for localized melting and material deposition makes the process highly sensitive to parameters, such as laser power, powder feed rate, scanning speed, melt pool temperature, and cooling rate [13–16,19,20]. Inappropriate parameter settings can result in melt pool instability, uneven deposition, excessive thermal stresses, porosity, cracking, lack of fusion, and other defects [15]. These issues are further intensified by the inherently dynamic thermal environment, often leading to non-uniform microstructures and inconsistent mechanical properties in the final part [15,19,20]. To overcome these challenges, in situ monitoring and closed-loop feedback control systems have been proposed to optimize process parameters and improve product quality [21–23]. Various sensing and monitoring techniques, such as image-based sensing [24–29], spectral analysis [30–32], X-ray imaging [33–35], and acoustic emission [36–39], offer distinct advantages but also face significant limitations. Complementary metal-oxide-semiconductor (CMOS) or charge-coupled device (CCD) cameras capture optical images to analyze melt pool geometry [24–26], but their performance can be compromised by laser radiation and intense light from the molten metal. Infrared cameras monitor thermal profiles and assist in defect prediction, though their accuracy depends on precise calibration to account for variations of emissivity across material surfaces [27–29]. Spectral analysis provides information about the melt pool and temperature, but is highly sensitive to ambient noise and demands complex calibration procedures [30–32]. X-ray imaging offers high accuracy for defect detection but is costly, time-intensive, and currently impractical for in situ monitoring and closed-loop control [33–35]. Audible sound techniques enable rapid defect detection but are sensitive to environmental noise and printing trajectory [38,39].

[1]Corresponding author.

Manuscript received June 17, 2025; final manuscript received November 12, 2025; published online December 4, 2025. Assoc. Editor: Dong Lin.

In this article, we develop two novel image-based methods—the contact angle (CA) method and the weighted mask (WM) method—for robust and rapid in-line monitoring of the balling phenomenon in the melt pool during DED processes. Figures 1(*a*) and 1(*b*) show the CAs with normal and balling pools, respectively. Irregularly shaped residual material may also appear ahead of the melt pool along the machine direction. This balling phenomenon occurs when the melt pool does not properly wet the substrate or the previously deposited layer, leading to invisible voids or irregularities in the final product. Both the CA and WM methods are implemented using high-speed videos, with the setup schematically shown in Fig. 1(*c*). For experimental validation, we compare the results of the WM method and the audible sound method from a previous study [39] with those obtained using the CA method, based on the same high-speed video dataset. The processing speeds of the CA and WM methods, 665 fps and 903 fps, respectively, demonstrate a potential for in-line monitoring and feedback control, especially when enhanced through parallel computing with multithreading or a higher-performance CPU.

## 2 Methodology

In this section, we describe the CA and WM methods. In the illustrations, the melt pool moves from left to right.

**2.1 Contact Angle Method.** The CA method predicts the balling phenomenon by extracting the CA between the melt pool and the substrate (or the previously deposited layer). The positions of the camera and laser head are fixed with respect to the melt pool during the process, allowing us to define a subregion of interest, shown in the boxed area in Fig. 2(*a*), to reduce computational cost. On the other hand, choosing a subregion helps the algorithm avoid influence from spatter and reflections of light between the melt pool and substrate. After this step, we convert the RGB image to a grayscale one with an eight-bit unsigned integer (unit8) format.

To obtain a binary image, a threshold is applied as a high-pass filter as

$$T_g = a \times I_{\max} \tag{1}$$

where $I_{\max}$ is the maximum grayscale intensity in the subregion. The values above the threshold are set to 1, and values below the threshold are set to 0. We choose $a = 0.8$ and obtain a resulting binary image, as shown in Fig. 2(*b*). The largest connected component within the subregion is then extracted using either "bwlabel" in MATLAB [40] or "cv::connectedComponents" in OPENCV. For each row in the resulting binary image, the rightmost nonzero pixels are selected and marked to form the set of rightmost points, as shown in Fig. 2(*c*).

Based on the resolution for this case, the five rightmost points closest to the substrate are selected to fit the line for calculating the CA. Those points are the rightmost points with the largest coordinate values in the $v$-direction. An iteratively reweighted least squares method is applied to remove outliers. This method iteratively computes residuals from a weighted least squares fitting (WLSF) and updates the weights assigned to each point based on a weighting formula (assigning smaller weights to points with larger residuals).

To perform the fitting, the WLSF utilizes the residual error function

$$J_w = \sum_{i=1}^{n} w_i (v_i - k u_i - b)^2 \tag{2}$$

where $w_i$ is the weight assigned to the $i$th point with image coordinates $(u_i, v_i)$, $k$ is the slope, and $b$ is the intercept. To minimize the residual error function, we have

$$\sum_{i=1}^{n} w_i (v_i - k u_i - b) = 0 \tag{3}$$

We rewrite Eq. (3) in matrix form and apply least square fitting as

$$\begin{Bmatrix} k & b \end{Bmatrix}^T = (\mathbf{U}^T \mathbf{W} \mathbf{U})^{-1} (\mathbf{U}^T \mathbf{W} \mathbf{V}) \tag{4}$$

where

$$\mathbf{U} = \begin{bmatrix} u_1 & 1 \\ u_2 & 1 \\ \vdots & \vdots \\ u_n & 1 \end{bmatrix}, \quad \mathbf{V} = \begin{bmatrix} v_1 \\ v_2 \\ \vdots \\ v_n \end{bmatrix}, \quad \mathbf{W} = \begin{bmatrix} w_1 & 0 & \cdots & 0 \\ 0 & w_2 & \cdots & 0 \\ \vdots & \vdots & \ddots & 0 \\ 0 & 0 & 0 & w_n \end{bmatrix}$$

We assign an initial weight of 1 to each point. At each iteration, the residual for each point is computed as

$$r_i = v_i - k u_i - b, \tag{5}$$

and the weights are updated using a simplified Cauchy weight function as

$$w_i = \frac{1}{1 + |r_i|} \tag{6}$$

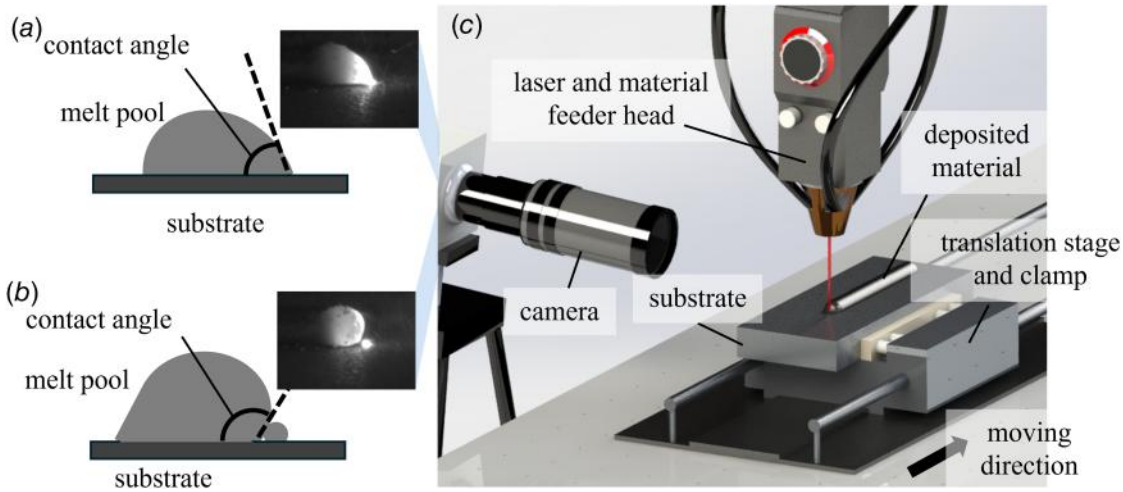


**Fig. 1 (*a*) Normal melt pool, (*b*) balling melt pool, and (*c*) schematic of the camera setup integrated with the DED machine**

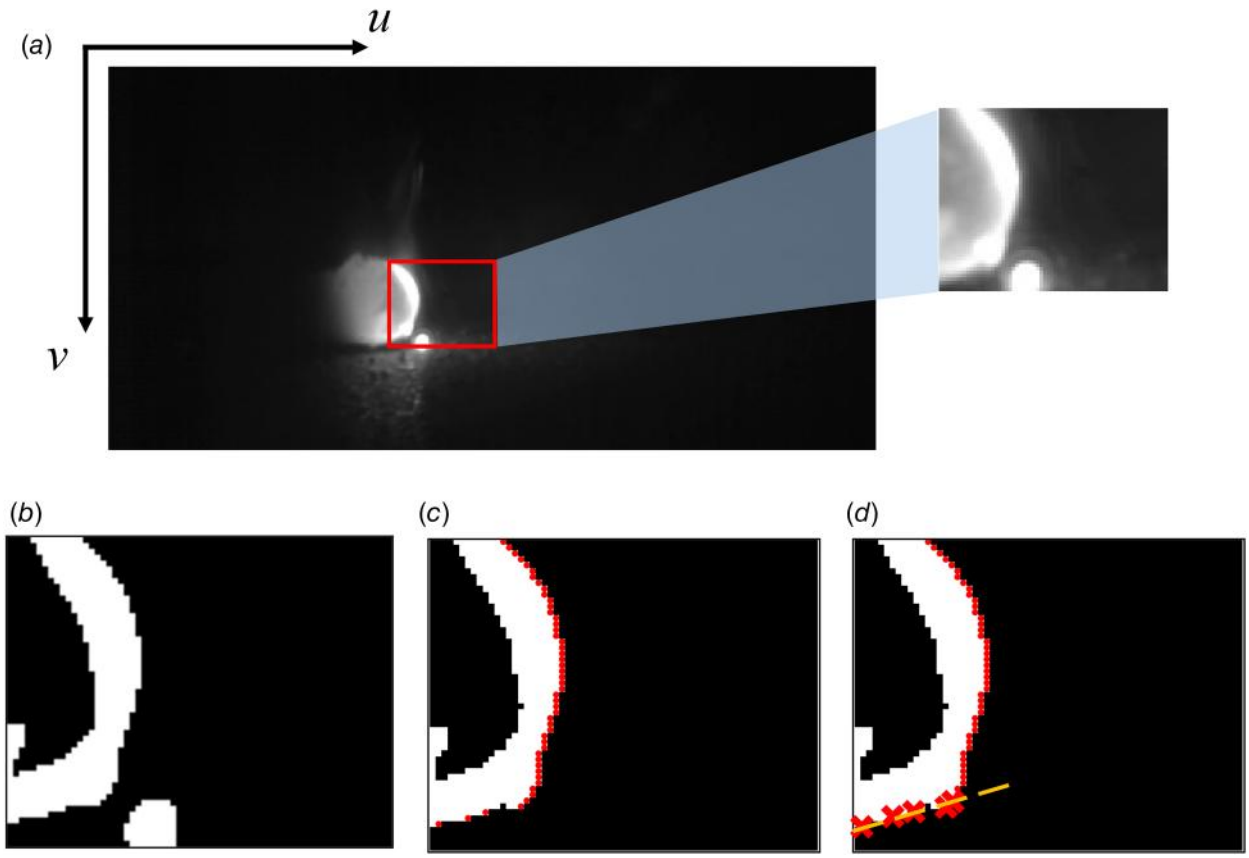


**Fig. 2 The workflow of the CA method: (*a*) original grayscale frame and enlarged subregion, (*b*) binary image of the subregion after thresholding, (*c*) the largest connected component with its rightmost points marked, and (*d*) points used for line fitting (shown as crosses) and the fitted line (dashed)**

The iteration process terminates when the residual drops below 0.01 or when the number of iterations exceeds 1000. Once the iterative process terminates, points with weights below a specified threshold (we choose 0.1 for this study) are considered outliers and are removed from the dataset. CA is then calculated from $k$ and serves as the primary indicator for judging the occurrence of balling. The selection of the threshold value will be discussed later in Sec. 4.

**2.2 Weighted Mask Method.** The WM method predicts balling by generating an evaluation number that reflects the likelihood of balling occurrence. The evaluation number is computed as

$$\delta = \sum_{i=1}^{m} \sum_{j=1}^{n} \mathbf{I}_b \odot \mathbf{M} \tag{7}$$

where $\mathbf{I}_b$ is an $m \times n$ binary matrix indicating the melt pool position within the subregion image, where pixels inside the melt pool are marked as 1 and those outside are marked as 0. $\odot$ is the Hadamard product (i.e., elementwise product) operator, and $\mathbf{M}$ is a WM matrix with the same size as the binary matrix.

This paragraph shows the process to determine $\mathbf{I}_b$. Due to the reflected halo around the melt pool, the grayscale intensity in the surrounding area may be higher than in some parts within the melt pool. Therefore, we divide the subregion into two parts (i.e., Parts 1 and 2 in Fig. 3(*a*)) and process them using different high-pass filter thresholds. Similar to the high-pass filter threshold used in the CA method, we apply $a = 0.8$ and $a = 0.4$ in Eq. (1) for Parts 1 and 2, respectively (Fig. 3(*b*)). Afterward, we fill the interior of the melt pool to obtain the desired binary matrix $\mathbf{I}_b$ representing the entire melt pool (Fig. 3(*c*)). This can be performed using functions such as "imfill" in MATLAB [40] or "floodFill"/"scipy.ndimage.binary" in OPENCV.

We use three representative melt pool shape cases and four divided parts, as shown in Fig. 4, in the WM matrix to optimize the entry values on a part-wise basis. The three cases are: (1) Case 1 with a small acute CA; (2) Case 2 with a noticeable concave shape in the middle of the leading edge, indicating a tendency toward an increased CA; and (3) Case 3 with a small residual separated from the main body and an obtuse CA. The four parts of the WM matrix are designed to help distinguish the three cases and are denoted as A, B, C, and Z. To reduce the effect of the reflected halo, we estimate the boundaries of each part by detecting edges in the binary images of the three cases. These binary images are generated using the same method we used to determine $\mathbf{I}_b$. Part A represents the main region of a regularly shaped melt pool. Part B corresponds to the increased height of the pool. Part C indicates the potentially missing portion of the melt pool, as observed in Cases 2 and 3. Part Z represents the background. A weight factor is assigned to each entry in the WM matrix and is denoted as $W_A$, $W_B$, $W_C$, or $W_Z$, depending on the corresponding part. $W_A$ and $W_B$ are positive with $W_A < W_B$, $W_C$ is negative, and $W_Z$ is zero. Based on this assignment, we expect the evaluation numbers to increase as the case number increases. Therefore, the critical evaluation number indicating the occurrence of balling can be determined from Eq. (7) corresponding to Case 1.

Optimizing the weight factors is necessary to differentiate between the various cases. To achieve clear distinctions, we establish constraints as (1) an evaluation number $\delta > 0$ for all the cases, (2) $\delta_2{:}\delta_1 > 2$, $\delta_3{:}\delta_1 > 3$, where the subscripts indicate the case numbers, and an objective function for optimization as

$$f = (\delta_2 - 2\delta_1)^2 + (\delta_3 - 3\delta_1)^2 \tag{8}$$


**Fig. 3 Process for obtaining the desired binary matrix: (*a*) subregion divided into two parts, (*b*) binary image after applying high-pass filter thresholds, and (c) binary image after filling the interior of the melt pool**

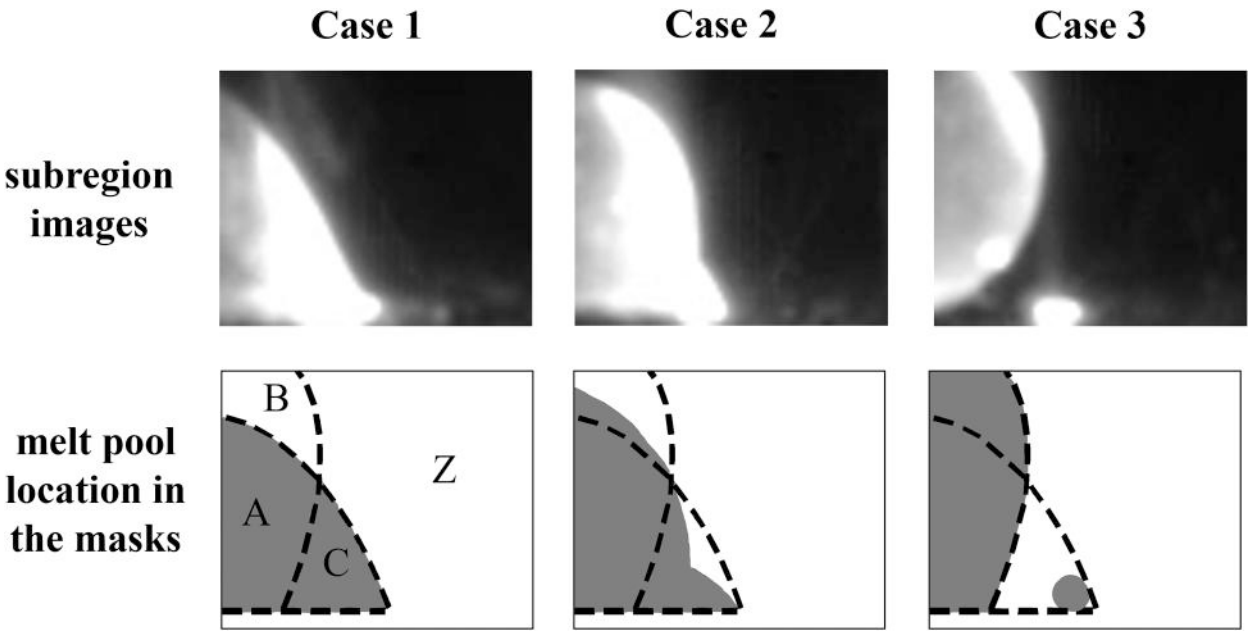


**Fig. 4 Three cases used for determining entry values in the WM matrix**

We provide an initial guess as $W_A = 1$, $W_B = 2$, and $W_C = -1$ to obtain the initial $\delta$ values. The MATLAB function "fmincon" [41] (equivalent alternatives as "NLopt" in C++ and "scipy.optimize.minimize" in PYTHON) is used to optimize $W_A$, $W_B$, and $W_C$ for a minimum $f$. With the three cases in Fig. 4, we obtain the ratios of these three values as

$$W_A{:}W_B{:}W_C = 1{:}1.328{:}-3.442 \tag{9}$$

The sensitivity of the results to the three representative cases chosen for optimization can be improved by increasing the ratio of $\delta_2$ to $\delta_1$ and the ratio of $\delta_3$ to $\delta_1$ specified in constraint (2), and by correspondingly modifying these ratios in Eq. (8).

## 3 Experimental Setup

Experiments were conducted on a DED additive manufacturing research platform setup in the Micro Manufacturing Laboratory at National Chung Hsing University, Taichung, Taiwan (Fig. 5). The platform is equipped with a YLR-500-MM-AC fiber laser (IPG Photonics, Oxford, MA) and a deposition system with a

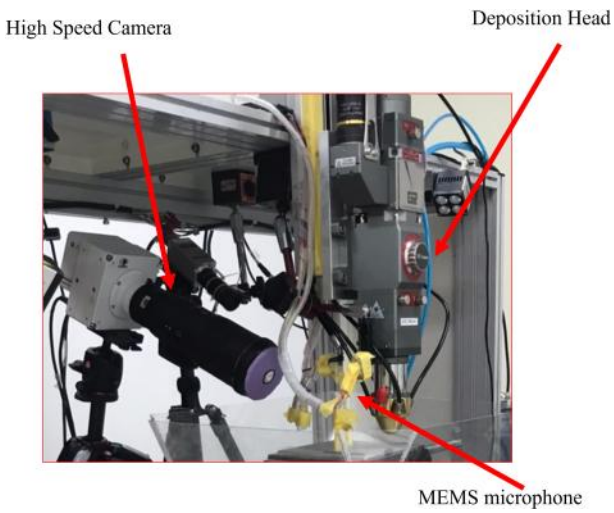


**Fig. 5 Experimental setup**

**Table 1 Process parameters and materials in the conducted experiments**

| Experimental type | Feed rate (mm/min) | Flowrate of powder (g/min) | Deposition length (mm) | Laser power (W) | Base material | Powder material |
|---|---|---|---|---|---|---|
| Line deposition | 60 | 7.09 | 10 | 116 | SUS304 | Inconel 718 ($\phi 50 \sim 150\ \mu$m) |

ECM340 powder delivery head (EC Laser, Kunshan, Jiangsu, China) and a DPSF-3 powder delivery system (GeniRay Technology Corporation, New Taipei City, Taiwan). The laser delivers up to 500 W of power at a wavelength of 1070 nm. Inconel 718 powder with particle diameters ranging from approximately 50 $\mu$m to 100 $\mu$m is used in the experiments. High-speed video is captured at 1000 fps using a VEO E310L optical camera (Phantom, Wayne, NJ) with a 532 nm green laser light source (Changchun New Industries Optoelectronics Tech. Co., Ltd., Changchun, Jilin, China). Simultaneously, acoustic data are collected using an SPM0408LE5H-TB MEMS microphone (Knowles, Itasca, IL), which has a frequency range of 100 Hz to 10 kHz, installed around the deposition spot. The microphone is installed 9 cm from the deposition location in the *XZ* plane, at a 60-degree angle to the deposition direction. Sound signals are collected and stored by a PXI 6132 data acquisition system (NI, Austin, TX) at a sampling rate of 2 MHz. After deposition, the profile of a deposited sample is measured and recorded using a VK-X1100 profiler (Keyence, Osaka, Japan) to evaluate surface conditions and dimensions. The material and deposition parameters adopted in this study are listed in Table 1 [39].

The images collected during the experiments are processed using MATLAB scripts on a computer with an AMD Ryzen™ 9 7940HS CPU (4.0 GHz, AMD, Santa Clara, CA). MATLAB is configured to utilize eight threads, which corresponds to the number used during processing. The video is stored on an SN850x 4TB solid-state drive (Western Digital, San Jose, CA), and all processing is performed entirely by the CPU without GPU acceleration.

## 4 Results and Discussions

We normalize the results from both the CA and WM methods. In the CA method, the CAs are normalized by dividing them by 180 deg. In the WM method, the evaluation numbers are normalized by dividing by a theoretical maximum value, which is derived from a hypothetical binary image where only Parts A and B are bright, and all other parts are dark. The CA method provides a direct and explicit indicator to detect the balling phenomenon based on physics, while the WM method offers an implicit manner.

In Fig. 6, we compare the CA and WM methods through two sets of results, presented together with audible sound signals and deposited height data reported in the previous research [39]. We define the criteria for detecting balling as follows: in the CA method, a contact angle greater than 90 deg or 0.5 after normalization, which means non-wetting [41], indicates balling; in the WM method, an evaluation number of 0.5 or higher indicates balling. The 0.5 criterion for the WM method is derived from the dataset shown in Fig. 6(*a*), where the maximum normalized evaluation number is approximately 0.75 (as observed in Case 3). Based on Constraint 2 that we established, Case 2 yields an evaluation number of 0.5, which we adopt as the threshold for balling detection. This criterion also proves effective when applied to the dataset in Fig. 6(*b*).

In Fig. 6(*a*), the CA method shows that there was one instance where the contact angle was greater than 90 deg. The WM also detected the instance. The audible sound method, however, could not detect the balling phenomenon. The sample characterization confirmed that this instance indeed resulted in the largest deposition height occurring around 4 s. In Fig. 6(*b*), the data from both CA and WM methods show that the process was fairly stable (mostly below threshold) from 13 s to 19 s. The deposition heights were also consistent. For an audible sound signal,

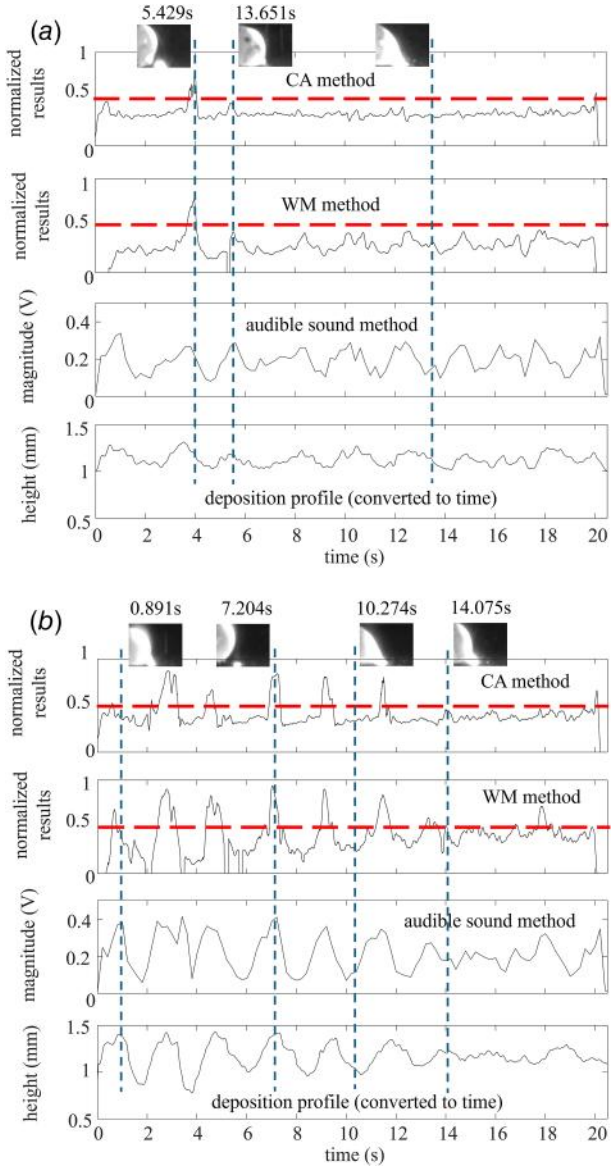


**Fig. 6 (*a*) and (*b*) Two sets of results obtained from four different methods**

however, it is difficult to establish a criterion to determine if the balling occurred during that time period.

Overall, the results from the CA and WM methods align well with each other and correspond closely to the outcomes from the audible sound method and deposition profile. The explicit CA method validates the results obtained from the audible sound signals. The results show that the audible sound method can predict balling slightly earlier, which is beneficial for implementing feedback control to mitigate the balling tendency. However, this method faces limitations due to its sensitivity to environmental noise and the placement of the microphone. The sound energy level depends closely on the difference between the deposition direction and the microphone orientation. The deposited height is measured after the process is complete and is used for comparison purposes.

In addition to the above results, we record the computational speeds of the CA and WM methods using eight threads on the previously mentioned CPU. The CA method achieves an average processing speed of 665 fps, with a minimum speed of 596 fps. In comparison, the WM method achieves an average speed of 903 fps, with a minimum of 702 fps, making it approximately 1.5 times faster than the CA method. The performance of both methods can be further improved through enhanced parallel computing using multithreading or a higher-performance CPU. For the WM method, implementing a sparse matrix representation can also increase computational efficiency. These results suggest that both methods are suitable for potential in-line monitoring applications.

Future work in this research may include implementing a machine learning approach to more precisely determine the optimal entries in the WM matrix on an entry-wise basis. This enhancement would further improve the WM method's ability to capture detailed melt pool features. Additionally, integrating a feedback control system into the DED process, by combining the CA or WM method with the audible sound method, could enable real-time mitigation of the balling phenomenon before it happens. As for the closed system, the parameters that can be used to control the surface profile are the laser power, the volume of the delivered powder, and the deposition spot size. The laser power can be modulated by adjusting the pulse duration, while the volume of delivered powder can be controlled through the feed rate. Additionally, the position of the deposition head (i.e., the distance between the base plate and the head) can be automatically adjusted to modify the spot size of both the laser and the powder simultaneously.

In addition, these methods can be extended to new materials or different processing workflows. The CA method requires no recalibration, making it readily applicable. In contrast, the WM method may require recalibration using three selected representative cases to generate new weighted masks. These masks can be validated using the CA method or through acoustic-based approaches.

## 5 Conclusion

We developed two image-based methods, i.e., the CA method and the WM method, to monitor the balling phenomenon in DED processes. The CA method detects balling by analyzing the melt pool's contact angle, while the WM method generates an evaluation number to assess balling severity. Experimental validation demonstrated that both methods effectively detect the balling phenomenon and show a strong correlation with results from an audible sound-based monitoring technique, as well as the post-processed deposition profile. Performance evaluation showed that the WM method achieved a higher average processing speed (903 fps) compared to the CA method (665 fps). Both methods show strong potential for integration into feedback control systems, enhancing process reliability and efficiency.


## Acknowledgment

This work was supported by DF's startup funding and by the Ministry of Science and Technology in Taiwan under Grant MOST 111-2634-F-007-010.


## Conflict of Interest

The authors declare that they have no known competing financial interests or personal relationships that could have appeared to influence the work reported in this article.

## Data Availability Statement

The datasets generated and supporting the findings of this article are obtainable from the corresponding author upon reasonable request.

## Author Contribution Statement

Yangyuan Li: conceptualization, methodology, software, writing—original draft, validation, visualization; Cong-Yue Wu: investigation, data curation, visualization; Ming-Chyuan Lu: conceptualization, data curation, resources, supervision, writing—review and editing; Jyhwen Wang: conceptualization, data curation, resources, supervision, writing—review and editing; Dan Feng: conceptualization, data curation, funding acquisition, investigation, methodology, project administration, resources, supervision, validation, visualization, writing—original draft, writing—review and editing.

## References


[1] Preis, J., Wang, Z., Howard, J., Lu, Y., Wannenmacher, N., Shen, S., Paul, B. K., and Pasebani, S., 2024, "Effect of Laser Power and Deposition Sequence on Microstructure of GRCop42-Inconel 625 Joints Fabricated Using Laser Directed Energy Deposition," Mater. Des., **241**, p. 112944.

[2] Liu, K., Yan, Z., Pan, R., Wang, X., Wang, F., and Chen, S., 2024, "Interfacial Bonding and Microstructural Evolution in Inconel-Copper Bimetallic Structures Fabricated by Directed Energy Deposition-Arc," Mater. Sci. Eng. A, **898**, p. 146381.

[3] Suresh, T., Landes, S., Letcher, T., Prasad, A., Gradl, P., and Ellis, D., 2020, "Nanomechanical Characterization of Additive Manufactured Grcop-42 Alloy Developed by Directed Energy Deposition Methods," ASME International Mechanical Engineering Congress and Exposition, American Society of Mechanical Engineers, Vol. 84515, p. V004T04A003.

[4] Jeong, J.-Y., Kang, H.-S., Kim, S.-H., Lee, K.-Y., Kim, D.-J., and Shim, D.-S., 2023, "Adhesion With Aluminum for Material Surfaces Additively Manufactured by Directed Energy Deposition," Int. J. Precis. Eng. Manuf. Green Technol., **10**(6), pp. 1579–1604.

[5] Koopmann, E. T., Jäger, T., Kaminsky, C., and Zeidler, H., 2025, "Development of Heating Strategies to Reduce Crack Formation in the Manufacturing Process of Tool Components Using Directed Energy Deposition," Prog. Addit. Manuf., **10**(3), pp. 1–9.

[6] Yi, H., Wang, Q., and Cao, H., 2022, "Wire-Arc Directed Energy Deposition of Magnesium Alloys: Microstructure, Properties and Quality Optimization Strategies," J. Mater. Res. Technol., **20**, pp. 627–649.

[7] Hattingh, D. G., Botha, S., Bernard, D., James, M. N., and du Plessis, A., 2022, "Corrosion Fatigue of Ti-6Al-4V Coupons Manufactured by Directed Energy Deposition," Fatigue Fract. Eng. Mater. Struct., **45**(7), pp. 1969–1980.

[8] Bajda, S., Cholewa-Kowalska, K., Krzyzanowski, M., Dziadek, M., Kopyscianski, M., Liu, Y., and Rai, A., 2024, "Laser-Directed Energy Deposition of Bioactive Glass on Ti-6Al-7Nb Titanium Alloy Substrate With Highly Refined Grain Structure," Surf. Coat. Technol., **485**, p. 130904.

[9] Pan, J., Wang, F., Xu, Z., Ma, S., Li, Y., and Gao, D., 2025, "Microstructure and Mechanical Properties of Ti-10Mo-xCu Alloy Additively Manufactured by Laser-Directed Energy Deposition Process," J. Mater. Eng. Perform., **34**(18), pp. 1–10.

[10] Wilson, J. M., Piya, C., Shin, Y. C., Zhao, F., and Ramani, K., 2014, "Remanufacturing of Turbine Blades by Laser Direct Deposition With Its Energy and Environmental Impact Analysis," J. Clean. Prod., **80**, pp. 170–178.

[11] Piscopo, G., and Iuliano, L., 2022, "Current Research and Industrial Application of Laser Powder Directed Energy Deposition," Int. J. Adv. Manuf. Technol., **119**(11), pp. 6893–6917.

[12] Saboori, A., Aversa, A., Marchese, G., Biamino, S., Lombardi, M., and Fino, P., 2019, "Application of Directed Energy Deposition-Based Additive Manufacturing in Repair," Appl. Sci., **9**(16), p. 3316.

[13] Ahn, D.-G., 2021, "Directed Energy Deposition (DED) Process: State of the art," Int. J. Precis. Eng. Manuf. Green Technol., **8**(2), pp. 703–742.

[14] Gibson, I., Rosen, D., Stucker, B., Gibson, I., Rosen, D., and Stucker, B., 2015, "Additive Manufacturing Technologies: 3D Printing, Rapid Prototyping, and Direct Digital Manufacturing." Johns. Matthey Technol. Rev., **59**(3), pp. 193–198.

[15] Svetlizky, D., Das, M., Zheng, B., Vyatskikh, A. L., Bose, S., Bandyopadhyay, A., Schoenung, J. M., Lavernia, E. J., and Eliaz, N., 2021, "Directed Energy Deposition (DED) Additive Manufacturing: Physical Characteristics, Defects, Challenges and Applications," Mater. Today, **49**, pp. 271–295.

[16] Svetlizky, D., Zheng, B., Vyatskikh, A., Das, M., Bose, S., Bandyopadhyay, A., Schoenung, J. M., Lavernia, E. J., and Eliaz, N., 2022, "Laser-Based Directed Energy Deposition (DED-LB) of Advanced Materials," Mater. Sci. Eng. A, **840**, p. 142967.

[17] Hariharan, K., Iams, A. D., Zuback, J. S., Palmer, T. A., Sridhar, N., Alazemi, R. M., Frankel, G. S., and Schindelholz, E. J., 2024, "Enhanced Localized Corrosion Resistance of Ni-Based Alloy 625 Processed by Directed Energy Deposition Additive Manufacturing," Corros. Sci., **230**, p. 111945.

[18] Song, L., Bagavath-Singh, V., Dutta, B., and Mazumder, J., 2012, "Control of Melt Pool Temperature and Deposition Height During Direct Metal Deposition Process," Int. J. Adv. Manuf. Technol., **58**(1–4), pp. 247–256.

[19] Liu, M., Kumar, A., Bukkapatnam, S., and Kuttolamadom, M., 2021, "A Review of the Anomalies in Directed Energy Deposition (DED) Processes & Potential Solutions-Part Quality & Defects," Proc. Manuf., **53**, pp. 507–518.

[20] Mo, B., Li, T., Deng, L., Shi, F., Liu, W., and Zhang, H., 2024, "Mechanisms and Influencing Factors of Defect Formations During Laser-Based Directed Energy Deposition With Coaxial Powder Feeding: A Review," Virtual Phys. Prototyp., **19**(1), p. e2404155.
[21] Zhang, X., Shen, W., Suresh, V., Hamilton, J., Yeh, L.-H., Jiang, X., Zhang, Z., et al., 2021, "In Situ Monitoring of Direct Energy Deposition Via Structured Light System and Its Application in Remanufacturing Industry," Int. J. Adv. Manuf. Technol., **116**(3), pp. 959–974.
[22] Tang, Z., Liu, W., Wang, Y., Saleheen, K. M., Liu, Z., Peng, S., Zhang, Z., and Zhang, H., 2020, "A Review on In Situ Monitoring Technology for Directed Energy Deposition of Metals," Int. J. Adv. Manuf. Technol., **108**(11–12), pp. 3437–3463.
[23] Haley, J., Karandikar, J., Herberger, C., MacDonald, E., Feldhausen, T., and Lee, Y., 2024, "Review of In Situ Process Monitoring for Metal Hybrid Directed Energy Deposition," J. Manuf. Process., **109**, pp. 128–139.
[24] Pandiyan, V., Cui, D., Parrilli, A., Deshpande, P., Masinelli, G., Shevchik, S., and Wasmer, K., 2022, "Monitoring of Direct Energy Deposition Process Using Manifold Learning and Co-Axial Melt Pool Imaging," Manuf. Lett., **33**, pp. 776–785.
[25] Mi, J., Zhang, Y., Li, H., Shen, S., Yang, Y., Song, C., Zhou, X., Duan, Y., Lu, J., and Mai, H., 2023, "In-Situ Monitoring Laser Based Directed Energy Deposition Process With Deep Convolutional Neural Network," J. Intell. Manuf., **34**(2), pp. 1–11.
[26] Lyu, J., Akhavan, J., Mahmoud, Y., Xu, K., Vallabh, C. K. P., and Manoochehri, S., 2023, "Real-Time Monitoring and Gaussian Process-Based Estimation of the Melt Pool Profile in Direct Energy Deposition," International Manufacturing Science and Engineering Conference, American Society of Mechanical Engineers, Vol. 87233, p. V001T01A024.
[27] Li, X., Siahpour, S., Lee, J., Wang, Y., and Shi, J., 2020, "Deep Learning-Based Intelligent Process Monitoring of Directed Energy Deposition in Additive Manufacturing With Thermal Images," Proc. Manuf., **48**, pp. 643–649.
[28] Paudel, B. J., Marshall, G., and Thompson, S., 2022, "Thermal Monitoring and Modeling of Ti–6Al–4V Thin Wall Temperature Distribution During Blown Powder Laser Directed Energy Deposition," ASME J. Manuf. Sci. Eng., **144**(4), p. 041007.
[29] Hagenlocher, C., O'Toole, P., Xu, W., Brandt, M., Easton, M., and Molotnikov, A., 2022, "In Process Monitoring of the Thermal Profile During Solidification in Laser Directed Energy Deposition of Aluminium," Addit. Manuf. Lett., **3**, p. 100084.
[30] Li, J., Duan, Q., Hou, J., Xie, H., and Liu, S., 2020, "In-Situ Monitoring of Substrate Deformation in Directed Energy Deposition Process Using the Coherent Gradient Sensing Method," Addit. Manuf., **36**, p. 101547.
[31] Kisielewicz, A., Sikström, F., Christiansson, A.-K., and Ancona, A., 2018, "Spectroscopic Monitoring of Laser Blown Powder Directed Energy Deposition of Alloy 718," Proc. Manuf., **25**, pp. 418–425.
[32] Hu, G., Zha, R., Wang, Y., Cao, J., and Guo, P., 2024, "Digital Fringe Projection for Interlayer Print Defect Characterization in Directed Energy Deposition," International Symposium on Flexible Automation, American Society of Mechanical Engineers, Vol. 87882, p. V001T01A002.
[33] Wolff, S. J., Wu, H., Parab, N., Zhao, C., Ehmann, K. F., Sun, T., and Cao, J., 2019, "In-Situ High-Speed X-ray Imaging of Piezo-Driven Directed Energy Deposition Additive Manufacturing," Sci. Rep., **9**(1), p. 962.
[34] Chen, Y., Clark, S. J., Collins, D. M., Marussi, S., Hunt, S. A., Fenech, D. M., Connolley, T., et al., 2021, "Correlative Synchrotron X-ray Imaging and Diffraction of Directed Energy Deposition Additive Manufacturing," Acta Mater., **209**, p. 116777.
[35] Wolff, S. J., Wang, H., Gould, B., Parab, N., Wu, Z., Zhao, C., Greco, A., and Sun, T., 2021, "In Situ X-ray Imaging of Pore Formation Mechanisms and Dynamics in Laser Powder-Blown Directed Energy Deposition Additive Manufacturing," Int. J. Mach. Tools Manuf., **166**, p. 103743.
[36] Whiting, J., Springer, A., and Sciammarella, F., 2018, "Real-Time Acoustic Emission Monitoring of Powder Mass Flow Rate for Directed Energy Deposition," Addit. Manuf., **23**, pp. 312–318.
[37] Li, S., Chen, B., Tan, C., and Song, X., 2024, "In Situ Identification of Laser Directed Energy Deposition Condition Based on Acoustic Emission," Opt. Laser Technol., **169**, p. 110152.
[38] Ansari, M. J., Arcondoulis, E. J. G., Roccisano, A., Schulz, C., Schlaefer, T., and Hall, C., 2024, "Optimized Analytical Approach for the Detection of Process-Induced Defects Using Acoustic Emission During Directed Energy Deposition Process," Addit. Manuf., **86**, p. 104218.
[39] Wu, C. Y., Lu, M. C., Yang, W. C., and Chi, N. C., 2024, "Experimental Study of Balling Defect Generation and Audible Sound Analysis in Directed Energy Deposition Metal Additive Manufacturing," Int. J. Adv. Manuf. Technol., **134**(1), pp. 205–221.
[40] The MathWorks Inc, 2024, *Image Processing Toolbox Version: 24.2 (R2024b)*, The MathWorks Inc, Natick, MA, https://www.mathworks.com
[41] Fowkes, F. M., 1964, *Contact Angle, Wettability, and Adhesion*, American Chemical Society, Washington, DC.